

Unexpected two-fold symmetric superconductivity in few-layer NbSe₂

Alex Hamill^{1†}, Brett Heischmidt^{1†}, Egon Sohn^{2,3†}, Daniel Shaffer¹, Kan-Ting Tsai¹, Xi Zhang¹, Xiaoxiang Xi⁴, Alexey Suslov⁵, Helmuth Berger⁶, László Forró⁶, Fiona J. Burnell¹, Jie Shan^{3,7}, Kin Fai Mak^{3,7}, Rafael M. Fernandes¹, Ke Wang^{1*} and Vlad S. Pribiag^{1*}

¹*School of Physics and Astronomy, University of Minnesota, Minneapolis, MN, USA*

²*Department of Physics, The Pennsylvania State University, University Park, PA, USA*

³*Department of Physics and School of Applied and Engineering Physics, Cornell University, Ithaca, NY, USA*

⁴*National Laboratory of Solid State Microstructures, School of Physics, and Collaborative Innovation Center of Advanced Microstructures, Nanjing University, Nanjing, China*

⁵*National High Magnetic Field Laboratory, Tallahassee, FL, USA*

⁶*Institute of Condensed Matter Physics, Ecole Polytechnique Fédérale de Lausanne, Lausanne, Switzerland*

⁷*Kavli Institute at Cornell for Nanoscale Science, Ithaca, NY, USA*

Two-dimensional transition metal dichalcogenides (TMDs) have been attracting significant interest^{1–8} due to a range of properties, such as layer-dependent inversion symmetry, valley-contrasted Berry curvatures, and strong spin-orbit coupling (SOC). Of particular interest is niobium diselenide (NbSe₂), whose superconducting state in few-layer samples is profoundly affected by an unusual type of SOC called Ising SOC⁷. Combined with the reduced dimensionality, the latter stabilizes the superconducting state against magnetic fields up to ~35 T and could lead to other exotic properties such as nodal and crystalline topological superconductivity^{9–14}. Here, we report transport measurements of few-layer NbSe₂ under in-plane external magnetic fields, revealing an unexpected two-fold rotational symmetry of the superconducting state. In contrast to the three-fold symmetry of the lattice, we observe that

*Corresponding authors: vpribiag@umn.edu, kewang@umn.edu

† These authors contributed equally

the magnetoresistance and critical field exhibit a two-fold oscillation with respect to an applied in-plane magnetic field. We find similar two-fold oscillations deep inside the superconducting state in differential conductance measurements on NbSe₂/CrBr₃ superconductor-magnet junctions. In both cases, the anisotropy vanishes in the normal state, demonstrating that it is an intrinsic property of the superconducting phase. We attribute the behavior to the mixing between two closely competing pairing instabilities, namely, the conventional s-wave instability typical of bulk NbSe₂ and an unconventional d- or p-wave channel that emerges in few-layer NbSe₂. Our results thus demonstrate the unconventional character of the pairing interaction in a few-layer TMD, opening a new avenue to search for exotic superconductivity in this family of 2D materials.

In the conventional BCS theory of superconductivity, the pairing state is characterized by the breaking of an U(1) symmetry related to fixing the phases of the Cooper-pairs wave-function. Yet, several superconductors break additional symmetries, leading to new forms of superconductivity. Symmetry breaking in a superconductor may arise through intrinsically anisotropic pairing channels, as well as through coupling between different channels promoted by external perturbations. Hexagonal NbSe₂ is a member of the transition metal dichalcogenide (TMD) family that exhibits superconductivity¹⁵ and charge-density wave order¹⁶⁻¹⁸ from bulk to monolayer forms. In bulk, NbSe₂ is believed to be in the s-wave pairing state¹⁹. However, in few-layer hexagonally-stacked 2H-NbSe₂, the underlying crystalline symmetries give rise to distinct electronic properties. For example, odd-layer-number NbSe₂ lacks inversion symmetry (Figures 1a,b), which leads to a spin-orbit interaction that polarizes the spins of different valleys in different out-of-plane directions⁷, as illustrated by the Fermi surface plotted in Figure 1c. This so-called Ising-SOC stabilizes the superconducting state against in-plane magnetic fields far exceeding the Pauli paramagnetic limit imposed by conventional superconducting theory^{20,21}. This effect

becomes stronger as the monolayer limit is approached^{7,22}. In addition to Ising superconductivity⁹⁻¹¹, other unique superconducting properties such as field-induced mixed-parity states^{23,24} and nodal topological superconductivity have been theoretically proposed^{12-14,25}. However, other than the stability of the superconducting state against high fields, little is known experimentally about the nature and symmetry of the pairing state in few-layer NbSe₂.

In this work, we report two-fold-periodic superconducting properties of few-layer encapsulated NbSe₂ samples studied under rotating in-plane magnetic fields. This periodicity is confirmed by three complementary experimental approaches: magneto-transport near the transition temperature (T_c), measurements of the critical field (H_c), and tunneling across magnetic tunnel junctions deep inside the superconducting state. The superconducting properties follow a $\cos(2\theta)$ dependence on the in-plane field angle as probed with all three experimental approaches. These results are suggestive of field- or strain-induced mixing between quasi-degenerate pairing states with s-wave and d- or p-wave symmetries in few-layer samples, thus shedding new light on the unusual superconducting state of few-layer TMDs.

Figure 1d shows Device 1 (schematic in Figure 1e), an hBN-encapsulated five-layer NbSe₂ sample, used for magneto-transport measurements. Figure 1g shows Device 2 (schematic in Figure 1h), a magnetic tunnel junction, which consists of a normal metal (Pt), bilayer CrBr₃ and trilayer NbSe₂. CrBr₃ with H-stacking is a magnetic semiconductor^{26,27} (gap 0.6-3.8 eV²⁸) with a ferromagnetic ordering temperature of 36 K²⁹ and a magnetic anisotropy field (as reflected by the in-plane saturation field) ~ 440 mT²⁹⁻³¹. For both types of devices, the NbSe₂ was exfoliated and encapsulated (see Methods for details) in Ar-filled gloveboxes (<0.1 ppm O₂ and H₂O concentration) to preserve a pristine nature for the NbSe₂ under study. The same approach was also followed for CrBr₃ in the case of the magnetic tunnel junctions.

Figure 1f shows the temperature-dependence of the resistance of Device 1. The sample shows a clear drop from the normal state resistance (R_N) to vanishing resistance, with a superconducting transition temperature $T_c \approx 5.0$ K (defined as the point where $R = 0.95R_N$). This value of T_c is consistent with the value of the superconducting gap extracted from tunneling data on 2D NbSe₂³². The device shows similar transport characteristics as those studied in Ref. 7: phonon-limited linear resistance ($R \propto T$) for high temperatures, indicating a metallic sample, and disorder-limited transport (R approaching a plateau) just above the superconducting transition. R_N is defined as the resistance value at this plateau. The resistance remains low (23.6 Ω) just above the superconducting drop, indicating the sample remains metallic all the way to the superconducting transition. Figure 1i shows similar four-probe data for the magnetic junction sample (Device 2). The four-probe resistance of the NbSe₂ flake measured as a function of temperature on a section non-overlapping with the CrBr₃ flake shows a superconducting transition with $T_c \approx 5.5$ K. The zero-bias differential conductance of the junction shows a similar onset temperature; however, the junction resistance saturates towards a finite value of 0.6 R_N due to the finite resistance of the CrBr₃ bilayer in series with the NbSe₂. The inset of Figure 1i shows the differential conductance (G) of the junction vs. d.c. bias at $T=1.9$ K. We fit the spectrum with the Blonder-Tinkham-Klapwijk (BTK) model, which considers both quasiparticle tunneling and Andreev reflection processes^{33,34}. The experimental data agree well with the fit except for the dip observed outside the superconducting gap. The small dip can be attributed to local heating in junctions with high transparency³⁵. The superconducting gap extracted from this fit, of about 0.67 meV, is comparable to the T_c value extracted from the resistance measurements.

Next, we discuss the magneto-transport properties of Device 1, probed under an in-plane magnetic field. Care was taken to rule out effects of an accidental out-of-plane component of the field (see Supplementary Sections 1, 2, 3, and 5). As the magnetic field is rotated in-plane ($\theta = 0$ corresponds to magnetic field aligned along the NbSe₂ flake's longest straight edge), we observe a pronounced two-

fold modulation of the magnetoresistance in the range between the onset and the offset of superconductivity (Figures 2a-e), which is consistent across multiple samples. Such a modulation is well described by a sinusoidal function of the form $\cos(2\theta + \varphi)$, as shown by the solid lines. As we varied the temperature for a fixed applied field amplitude of 8T, the angular modulation of the resistance (ΔR) was suppressed when the resistance was outside of the superconducting transition region (see Figure 2d). The phase of the oscillating signal also shifted slightly in Device 1 as a function of field and temperature (most apparent in Figures 2b and 2e). The field angles at which the resistance maxima or minima were observed were not affected by the directions of voltage measurement, current, and material transfer. However, the field angle of minimum resistance does show a consistent alignment with the long straight edge of the crystal (see Supplementary Section 5). We expect the long straight edge may be associated with the direction of cleaving during exfoliation, which may align along the zigzag (\vec{a}) or armchair (\vec{b}) directions.

The measurements described above were performed around T_c , in a temperature regime where superconducting fluctuations are present. To verify that this effect persists at lower temperatures, a similar 5-layer device (Device 3, $T_c \approx 6.4\text{K}$) was studied at a temperature of 0.5 K in fields up to $\sim 35\text{T}$, revealing a similar modulation of the magneto-resistance with applied field angle (Figure 2c and Supplementary Figure S4). For this device, we also studied the angular dependence of the critical field H_c that suppresses superconductivity, defined as the field at which the resistance is $0.5 R_N$ (measured at $T = 0.5\text{K}$). $H_c(\theta)$ also showed two-fold periodicity (Figure 2c). The oscillations of $H_c(\theta)$ and the magnetoresistance have a π phase shift, such that at angles where superconductivity is hardest to suppress, H_c is largest and the magnetoresistance is lowest, as expected. Importantly, these data indicate that the angle-dependence of the magnetoresistance is a good proxy for the angle-dependence of H_c .

To examine the possibility that small out-of-plane field contributions arising from misalignment could lead to these observations, the magneto-transport measurements were repeated in a canted configuration where the sample was intentionally canted by $\sim 7-9$ degrees out of the field rotation plane. The magnetoresistance oscillations in the canted configuration show a $|\sin(\theta)|$ form, as expected from geometric considerations, which is in contrast with the $\cos(2\theta + \varphi)$ dependence reported in the absence of canting (see Supplementary Section 1).

To confirm that the two-fold anisotropic features also emerge deep inside the superconducting state, we also studied the NbSe₂/CrBr₃ junction (Device 2). In particular, we measured the differential conductance spectra under a 3T in-plane magnetic field as a function of the angle θ , defined in the same manner as for Device 1. We also studied a second type of junction with a ferromagnetic (Co/Pt multilayer) electrode (Device 4) (see Supplementary Section 7). At 3T, the value of the applied field is expected to be substantially larger than the in-plane saturation field (~ 440 mT)²⁹ for few-layer CrBr₃, ensuring that its spins are oriented in the plane. Figure 3a summarizes the spectra in a color plot and shows a clear two-fold modulation, especially prominent at low bias smaller than or comparable to the superconducting gap. The angular dependence of the differential conductance at a fixed bias shows a clear contrast between biases larger or smaller than the gap (Figure 3b). The normalized differential conductance at energies outside the gap ($V=4\text{mV} > \Delta/e$) has less than a 0.5% variation vs. angle, indicating negligible anisotropic differential conductance. In contrast, the angular dependence of the normalized conductance at energies inside the gap ($V = 0$ mV) shows a clear two-fold modulation which can be fit to a $\cos(2\theta + \varphi)$ form (solid curve in Figure 3b). Overall, this indicates that the two-fold modulation persists deep inside the superconducting state of NbSe₂, consistent with the magneto-resistance and H_c behavior.

The differential conductance spectra at $\theta = 45^\circ$ and 135° (Figures 3c,d) show the variation of the angular dependence vs. field amplitude. At $H=0$, we observe a large differential conductance at low bias,

approaching 1.6 times the normal state value. This is due to a combination of Andreev reflection and quasiparticle tunneling at the junction. When a finite magnetic field is directed along $\theta = 45^\circ$, the differential conductance becomes greatly suppressed. In contrast, when the magnetic field is directed along $\theta = 135^\circ$, the conductance does not change appreciably compared to that of 0 T, indicating a higher resilience of the superconducting state to magnetic fields at this angle, and highlighting the two-fold anisotropy of this state. Note that due to the ferromagnetism of CrBr_3 , we expect magnetic proximity to be present at the $\text{CrBr}_3/\text{NbSe}_2$ interface³⁶, enhancing the effect of the applied magnetic field. In previous studies by some of us³⁴, we have investigated over ten bilayer and trilayer NbSe_2 tunnel junctions with nonmagnetic insulating barriers and electrodes under an arbitrary in-plane magnetic field direction relative to the NbSe_2 edge and have observed a monotonically decreasing gap from zero field up to the upper critical field ($\sim 38\text{T}$). In all devices, the spectra evolved in a manner qualitatively identical to that in Figure 3d, implying there is no strong angle dependence of the tunneling spectra without magnetic barriers and electrodes. Similarly, any out-of-plane magnetic field due to misalignment would also lead to a monotonically decreasing gap and therefore cannot result in the large suppression of zero bias differential conductance and widening of the spectra under magnetic field observed in this study (Figure 3c). The strong two-fold angular periodicity of the tunneling spectra is unique to devices with a magnetic insulating barrier (Device 2) or a magnetic electrode (see Supplementary Section 7).

Having experimentally established the two-fold anisotropic character of the superconducting state of few-layer NbSe_2 , we now discuss its possible origin. One scenario is that the superconducting state spontaneously breaks the three-fold rotational symmetry of the lattice, i.e. it is a nematic pairing state, similar to that observed in doped Bi_2Se_3 ³⁷. This is only possible if two conditions are satisfied: (i) the gap function transforms as the E' or E'' irreducible representations of the D_{3h} point group associated with the single-layer NbSe_2 crystal structure (which correspond roughly to d-wave and p-wave gaps, respectively), and (ii) the d-wave/p-wave nematic gap configuration has a lower energy than the d-

wave/p-wave chiral gap configuration. However, the facts that the superconducting state of bulk NbSe₂ is s-wave¹⁹ (i.e. it transforms as the A_1' irreducible presentation of D_{3h}), and that T_c seems to continuously and slowly change as a function of the number of layers⁷, pose a significant challenge to this scenario.

How could then an s-wave pairing state display two-fold anisotropy? One interesting possibility is that a small external symmetry-breaking field induces a strong mixing between the leading s-wave (A_1') instability and a sub-leading instability with either d-wave (E') or p-wave (E'') character. Such a strong mixing is of course only possible if these sub-leading instabilities of unconventional character, which presumably are accentuated in few-layer NbSe₂ due to the prominent role played by Ising SOC, are close competitors to the conventional s-wave instability, which presumably is inherited from the pairing mechanism of the crystal in bulk form. Note that the mixing discussed here is different than the singlet-triplet mixing that naturally occurs due to the presence of Ising SOC in the absence of external fields (see Supplementary Section 8). In our setup, two strong candidates exist for such an external symmetry-breaking field. Uniaxial strain mixes the s-wave (A_1') and d-wave (E') gaps^{38,39}, giving rise to an overall two-fold anisotropic gap. This is illustrated in Figure 4b, which shows the mixed gap along the Γ Fermi surface shown in Figure 1c (details in the Supplementary Section 8). Its two-fold anisotropy contrasts with the six-fold anisotropy of the s-wave gap shown in Figure 4a. Experimentally, residual uniaxial strain could arise for instance due to the exfoliation or encapsulation processes. The applied in-plane magnetic field itself also mixes different gap states, as was shown in Ref.23: due to the presence of the Ising SOC, it mixes the singlet component of the s-wave (A_1') gap with the triplet component of the p-wave (E'') gap, giving rise to a two-fold symmetric gap, illustrated in Figure 4c. We found that the two-fold anisotropy of the s+p mixed state is generally weaker than in the s+d mixed state, which can be seen here by comparing Figures 4b and 4c.

Insets in Figure 4 provide cartoon pictures of the possible s+p ($A_1'+E''$) and s+d ($A_1'+E'$) mixed states and their underlying symmetry-breaking fields. While a microscopic calculation connecting the anisotropic magneto-resistance, critical field, and tunneling data presented here with a specific form of the gap function is beyond the scope of this work, we expect that the two-fold anisotropy of the mixed gap function – and of the corresponding spectrum of superconducting fluctuations⁴⁰ – will be generally manifested as two-fold anisotropic superconducting properties.

Regardless of which scenario is realized here – spontaneous nematic superconductivity or strong gap-mixing triggered by a small symmetry-breaking field – our results point to a significant contribution of an unconventional pairing mechanism to the superconducting state of few-layer NbSe₂. This raises fundamental questions about the origin of such pairing interactions, and opens up fascinating prospects of combining them with non-trivial topological properties that have been predicted in the regime of high magnetic fields. Overall, our work reveals that few-layer TMDs provide a promising framework to realize and explore unconventional superconductivity.

Methods:

Device fabrication

For the magneto-transport and critical field measurement devices, Cr/PdAu (1nm/7nm) bottom contacts were deposited on top of an atomically-clean piece of hexagonal boron nitride (h-BN) of thickness 20-80nm, above which a piece of 2H-NbSe₂ (commercial, from HQ Graphene) and h-BN (20-80nm) was subsequently transferred using the standard dry-transfer technique³⁷. The NbSe₂ layer number was determined through optical contrast⁴¹ calibrated by atomic-force microscopy. The NbSe₂ exfoliation and subsequent hBN-encapsulation is performed in an Ar-filled glovebox to minimize sample degradation. After completing the assembly process, the van der Waals (vdW) heterostructure was taken out of the glove box and etched using reactive ion etching with O₂/Ar/CHF₃ to open windows on

the top h-BN for contacting the pre-patterned bottom contacts. Metal leads of Cr/Pd/Au (1nm/5nm/120nm) were subsequently deposited to connect the bottom contacts to the bonding pads.

For the junction devices, 2H-NbSe₂ bulk single crystals were prepared by the iodine-based chemical vapour transport method. CrBr₃ and hexagonal boron nitride (h-BN) bulk single crystals were grown by HQ graphene. NbSe₂ and CrBr₃ were thinned down by the conventional Scotch tape method and assembled by dry transfer technique^{42,43}. In detail, both NbSe₂ and CrBr₃ was first exfoliated on a polydimethylsiloxane (PDMS) polymer substrate. NbSe₂ flakes on the PDMS stamp were transferred to a Si/SiO₂ (295 nm) substrate which was heated to 70 °C. By searching with an optical microscope, trilayer NbSe₂ was identified. A stamp with a thin layer of polypropylene carbonate (PPC) on PDMS was prepared on a glass slide. The trilayer NbSe₂ was picked up to the stamp at 45 °C. Thin CrBr₃ flakes were identified on the PDMS polymer substrate and aligned to the NbSe₂ flake on the stamp. The CrBr₃ was picked up from the PDMS substrate to the stamp at 50 °C. The stack was aligned and approached to a pre-patterned metal electrode at 50 °C followed by heating the substrate to 120 °C in order to release the stack. The pre-patterned metal electrodes of Ti (3nm)/Pt (70nm) were prepared by standard photolithography and electron-beam evaporation. The PPC layer on the device was dissolved by anisole. Lastly, the device was single-side encapsulated by h-BN to prevent any degradation in air. All device fabrication procedures occurred in the glove box.

Measurements

The magneto-resistance measurements for Device 1 were performed using a Physical Properties Measurement System equipped with a rotating, variable-temperature sample insert and a 9T magnet. A standard lock-in technique was used with an a.c. current of 400 nA (3 μA was used for the R vs. T in Fig 1f only). Device 3 measurements were performed at the National High Magnetic Field Laboratory (NHMFL) in Tallahassee, FL, using a standard lock-in technique in a He³ cryostat equipped with a rotating sample insert and a 35T d.c. magnet. For the measurements at NHMFL, an a.c. current of 1 μA was used.

The junction devices were measured in a separate 9T Physical Property Measurement System at 1.9 K. A rotating probe was used to apply in-plane magnetic field in an angle θ . For the four-probe transport measurement of NbSe₂, we chose four electrodes which are in contact with NbSe₂ uncovered by CrBr₃. A standard lock-in technique was used with an a.c. current of 1 μ A. For the differential conductance measurements, a small a.c. current and d.c. bias current were generated by a lock-in amplifier and a d.c. voltage source meter, respectively, with load resistances in series. The superimposed current flowed through one of the split electrodes of the junction. The a.c. and d.c. voltages were measured between the other split electrode and another remote electrode using a pre-amplifier, lock-in amplifier and a voltage meter (see Supplementary Section 6 for measurement schematics). The amplitude of the a.c. voltage was kept below 50 μ A and d.c. voltage was varied from -8 mV to 8 mV. The differential conductance G was calculated from the ratio of the a.c. current to the measured a.c. voltage. The bias voltage V in the main text corresponds to the measured d.c. voltage.

Acknowledgements

We thank Eun-Ah Kim for useful discussions. B.H. and A.H. would like to thank Dave Graf and Scott Maier for their discussions and support related to work done at the National High Magnetic Field Laboratory. Special thanks also to Zhen Jiang for all of the support associated with the Physical Property Measurement System at UMN. The work at UMN was supported primarily by the National Science Foundation (NSF) Materials Research Science and Engineering Center at the University of Minnesota under Award No. DMR-1420013, via an iSuperSeed Award. Portions of the UMN work were conducted in the Minnesota Nano Center, which is supported by the National Science Foundation through the National Nano Coordinated Infrastructure Network (NNCI) under Award Number ECCS-1542202. A portion of this work was performed at the National High Magnetic Field Laboratory, which is supported by National Science Foundation Cooperative Agreement No. DMR-1644779 and the State of Florida. The

research at Cornell was supported by the Office of Naval Research (ONR) under award N00014-18-1-2368 for the tunneling measurements, and the National Science Foundation (NSF) under award DMR-1807810 for the fabrication of tunnel junctions. The work in Lausanne was supported by the Swiss National Science Foundation. K.F.M. also acknowledges support from a David and Lucille Packard Fellowship.

Author contributions

B.H., A.H., V.S.P. and K.W. designed the magnetoresistance and critical field experiments. B.H. performed the transport measurements at UMN with support from A.H. and K.T. B.H. and A.H. performed the measurements at the NHMFL with support from A.S. B.H. analyzed the data with support from A.H. under the supervision of V.S.P and K.W. A.H., K.T and X.Z. fabricated the magneto-transport heterostructures with support from B.H., under the supervision of K.W. Analytical modeling was performed by D.S., R.M.F. and F.J.B., who also contributed to the interpretation of the results. E.S., J.S. and K.F.M. designed the junction experiments. E.S. and X.X. fabricated and measured the junctions under the supervision of J.S. and K.F.M. E.S. analyzed the junction data under the supervision of J.S. and K.F.M., with input from V.S.P. and R.M.F. H.B. and L.F. grew the bulk NbSe₂ samples for tunnel junction studies. B.H., A.H., E.S., D.S., V.S.P. and R.M.F. co-wrote the manuscript. All authors discussed the results and provided comments on the manuscript.

Competing interests

The authors declare no competing interests.

Additional information

Supplementary information is available for this paper at [URL inserted by publisher]

Correspondence and requests for materials should be addressed to V.S.P. (vpribiag@umn.edu) and K.W. (kewang@umn.edu).

Data availability

All data needed to evaluate the conclusions in the paper are available from the corresponding author upon reasonable request.

Code availability

All relevant codes needed to evaluate the conclusions in the paper are available from the corresponding author upon reasonable request.

References

1. Xiao, D., Liu, G. Bin, Feng, W., Xu, X. & Yao, W. Coupled spin and valley physics in monolayers of MoS₂ and other group-VI dichalcogenides. *Phys. Rev. Lett.* **108**, (2012).
2. Mak, K. F., He, K., Shan, J. & Heinz, T. F. Control of valley polarization in monolayer MoS₂ by optical helicity. *Nat. Nanotechnol.* **7**, 494–498 (2012).
3. Zeng, H., Dai, J., Yao, W., Xiao, D. & Cui, X. Valley polarization in MoS₂ monolayers by optical pumping. *Nat. Nanotechnol.* **7**, 490–493 (2012).
4. Mak, K. F., McGill, K. L., Park, J. & McEuen, P. L. The valley hall effect in MoS₂ transistors. *Science (80-.)*. **344**, 1489–1492 (2014).
5. Jones, A. M. *et al.* Spin-layer locking effects in optical orientation of exciton spin in bilayer WSe₂. *Nat. Phys.* **10**, 130–134 (2014).
6. Riley, J. M. *et al.* Direct observation of spin-polarized bulk bands in an inversion-symmetric semiconductor. *Nat. Phys.* **10**, 835–839 (2014).
7. Xi, X. *et al.* Ising pairing in superconducting NbSe₂ atomic layers. *Nat. Phys.* **12**, 139–143 (2016).
8. Xu, X., Yao, W., Xiao, D. & Heinz, T. F. Spin and pseudospins in layered transition metal dichalcogenides. *Nat. Phys.* **10**, 343–350 (2014).
9. Yuan, N. F. Q., Mak, K. F. & Law, K. T. Possible topological superconducting phases of MoS₂. *Phys. Rev. Lett.* **113**, 097001 (2014).
10. Zhou, B. T., Yuan, N. F. Q., Jiang, H. L. & Law, K. T. Ising superconductivity and Majorana fermions in transition-metal dichalcogenides. *Phys. Rev. B* **93**, 180501 (2016).
11. Hsu, Y. T., Vaezi, A., Fischer, M. H. & Kim, E. A. Topological superconductivity in monolayer transition metal dichalcogenides. *Nat. Commun.* **8**, 1–6 (2017).
12. He, W.-Y. *et al.* Magnetic field driven nodal topological superconductivity in monolayer transition metal dichalcogenides. *Commun. Phys.* **1**, 40 (2018).
13. Fischer, M. H., Sigrist, M. & Agterberg, D. F. Superconductivity without Inversion and Time-Reversal Symmetries. *Phys. Rev. Lett.* **121**, 157003 (2018).
14. Shaffer, D., Kang, J., Burnell, F. J. & Fernandes, R. M. Crystalline Nodal Topological Superconductivity and Bogolyubov Fermi Surfaces in Monolayer NbSe₂. *arXiv:1904.05470* (2019).

15. Revolinsky, E., Lautenschlager, E. P. & Armitage, C. H. Layer structure superconductor. *Solid State Commun.* **1**, 59–61 (1963).
16. Ugeda, M. M. *et al.* Characterization of collective ground states in single-layer NbSe₂. *Nat. Phys.* **12**, 92–97 (2016).
17. Moncton, D. E., Axe, J. D. & DiSalvo, F. J. Neutron scattering study of the charge-density wave transitions in 2H-TaSe₂ and 2H-NbSe₂. *Phys. Rev. B* **16**, 801–819 (1977).
18. Harper, J. M. E., Geballe, T. H. & DiSalvo, F. J. Thermal properties of layered transition-metal dichalcogenides at charge-density-wave transitions. *Phys. Rev. B* **15**, 2943–2951 (1977).
19. Fletcher, J. D. *et al.* Penetration Depth Study of Superconducting Gap Structure of 2H-NbSe₂. *Phys. Rev. Lett.* **98**, 057003 (2007).
20. Clogston, A. M. Upper Limit for the Critical Field in Hard Superconductors. *Phys. Rev. Lett.* **9**, 266 (1962).
21. Chandrasekhar, B. S. A Note on the Maximum Critical Field of High-Field Superconductors. *Appl. Phys. Lett.* **1**, 7 (1962).
22. De La Barrera, S. C. *et al.* Tuning Ising superconductivity with layer and spin-orbit coupling in two-dimensional transition-metal dichalcogenides. *Nat. Commun.* **9**, 1427 (2018).
23. Möckli, D. & Khodas, M. Magnetic-field induced s⁺ if pairing in Ising superconductors. *Phys. Rev. B* **99**, 180505 (2019).
24. Möckli, D. & Khodas, M. Robust parity-mixed superconductivity in disordered monolayer transition metal dichalcogenides. *Phys. Rev. B* **98**, 144518 (2018).
25. Samokhin, K. V. Symmetry and topology of two-dimensional noncentrosymmetric superconductors. *Phys. Rev. B* **92**, 174517 (2015).
26. Tsubokawa, I. On the Magnetic Properties of a CrBr₃ Single Crystal. *J. Phys. Soc. Japan* **15**, 1664–1668 (1960).
27. Ghazaryan, D. *et al.* Magnon-assisted tunnelling in van der Waals heterostructures based on CrBr₃. *Nat. Electron.* **1**, 344–349 (2018).
28. Baral, D. *et al.* Multi-peak Electronic Density of States in CrBr₃ Revealed by Scanning Tunneling Microscopy. *arXiv:1909.00074* (2019).
29. Kim, H. H. *et al.* Evolution of interlayer and intralayer magnetism in three atomically thin chromium trihalides. *Proc. Natl. Acad. Sci. U. S. A.* **166**, 11131–11136 (2019).
30. Zhang, Z. *et al.* Direct Photoluminescence Probing of Ferromagnetism in Monolayer Two-Dimensional CrBr₃. *Nano Lett.* **19**, 3138–3142 (2019).
31. Chen, W. *et al.* Direct observation of van der Waals stacking–dependent interlayer magnetism. *Science (80-.).* **366**, 983–987 (2019).
32. Dvir, T. *et al.* Spectroscopy of bulk and few-layer superconducting NbSe₂ with van der Waals tunnel junctions. *Nat. Commun.* **9**, 1–6 (2018).
33. G. E. Blonder, M. Tinkham, and T. M. K. Transition from metallic to tunneling regimes in superconducting microconstrictions: Excess current, charge imbalance, and supercurrent conversion. *Phys. Rev. B* **25**, 4515–4532 (1982).
34. Sohn, E. *et al.* An unusual continuous paramagnetic-limited superconducting phase transition in 2D NbSe₂. *Nat. Mater.* **17**, 504–508 (2018).
35. Sheet, G., Mukhopadhyay, S. & Raychaudhuri, P. Role of critical current on the point-contact Andreev reflection spectra between a normal metal and a superconductor. *Phys. Rev. B* -

- Condens. Matter Mater. Phys.* **69**, 134507 (2004).
36. Cai, X. *et al.* Disentangling spin-orbit coupling and local magnetism in a quasi-two-dimensional electron system. *Phys. Rev. B* **100**, 081402(R) (2019).
 37. Matano, K., Kriener, M., Segawa, K., Ando, Y. & Zheng, G. Q. Spin-rotation symmetry breaking in the superconducting state of $\text{Cu}_x\text{Bi}_2\text{Se}_3$. *Nat. Phys.* **12**, 852–854 (2016).
 38. Fernandes, R. M. & Millis, A. J. Nematicity as a probe of superconducting pairing in iron-based superconductors. *Phys. Rev. Lett.* **111**, 127001 (2013).
 39. Kang, J., Kemper, A. F. & Fernandes, R. M. Manipulation of Gap Nodes by Uniaxial Strain in Iron-Based Superconductors. *Phys. Rev. Lett.* **113**, 217001 (2014).
 40. Venderbos, J. W. F., Kozii, V. & Fu, L. Identification of nematic superconductivity from the upper critical field. *Phys. Rev. B* **94**, 094522 (2016).
 41. Bing, D. *et al.* Optical contrast for identifying the thickness of two-dimensional materials. *Opt. Commun.* **406**, 128–138 (2018).
 42. Novoselov, K. S. *et al.* Electric field in atomically thin carbon films. *Science* (80-.). **306**, 666–669 (2004).
 43. Castellanos-Gomez, A. *et al.* Deterministic transfer of two-dimensional materials by all-dry viscoelastic stamping. *2D Mater.* **1**, 011002 (2014).

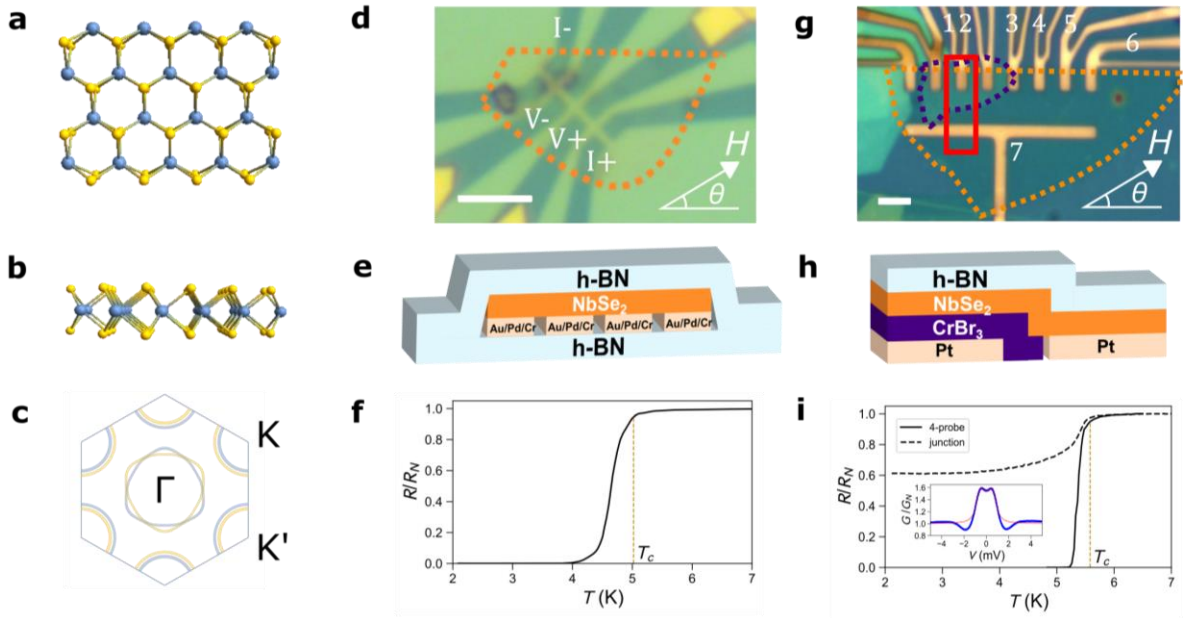


Fig. 1. Crystal structure, device layout and characterization. **a,b.** Top and side views of single-layer 2H-NbSe₂ crystal structure, respectively. Odd-layer NbSe₂ belongs to the point group D_{3h}. **c.** Single-layer NbSe₂ Fermi surface in the normal state. The yellow and blue lines represent the spin-split Fermi surface, with each subband corresponding to opposite out-of-plane spin orientations. **d.** Optical image of the 5-layer NbSe₂ device (Device 1) used for magnetoresistance measurements (scale bar: 5 μm). Contacts used for magnetoresistance measurements in Figure 2 are indicated. **e.** Diagrammatic cross section of Device 1. **f.** Superconducting transition for Device 1 ($R_N = 23.6 \Omega$) at $\mu_0 H = 0$. T_c is defined as the temperature at which $R = 0.95R_N$. **g.** Optical image of the 3-layer NbSe₂ and bilayer CrBr₃ device (Device 2) used for junction studies (scale bar: 5 μm). Contacts 1, 2, 4, and 7 were used in the junction study. Contacts 3, 4, 5, and 6 were used in the four-probe measurement. For Devices 1 and 2, θ is defined as the angle of the magnetic field with respect to the long straight edge of the NbSe₂ crystal (see **d** and **g**, orange outline). **h.** Diagrammatic cross section of Device 2. **i.** R vs. T for Device 2, showing junction resistance ($R_N = 266 \Omega$) and 4-probe resistance ($R_N = 30.6 \Omega$) at $\mu_0 H = 0$. The junction resistance has a sharp drop at the superconducting transition. Inset: Differential conductance (blue) and fit to the BTK model (red), indicating a superconducting gap of 0.67 meV, comparable to T_c .

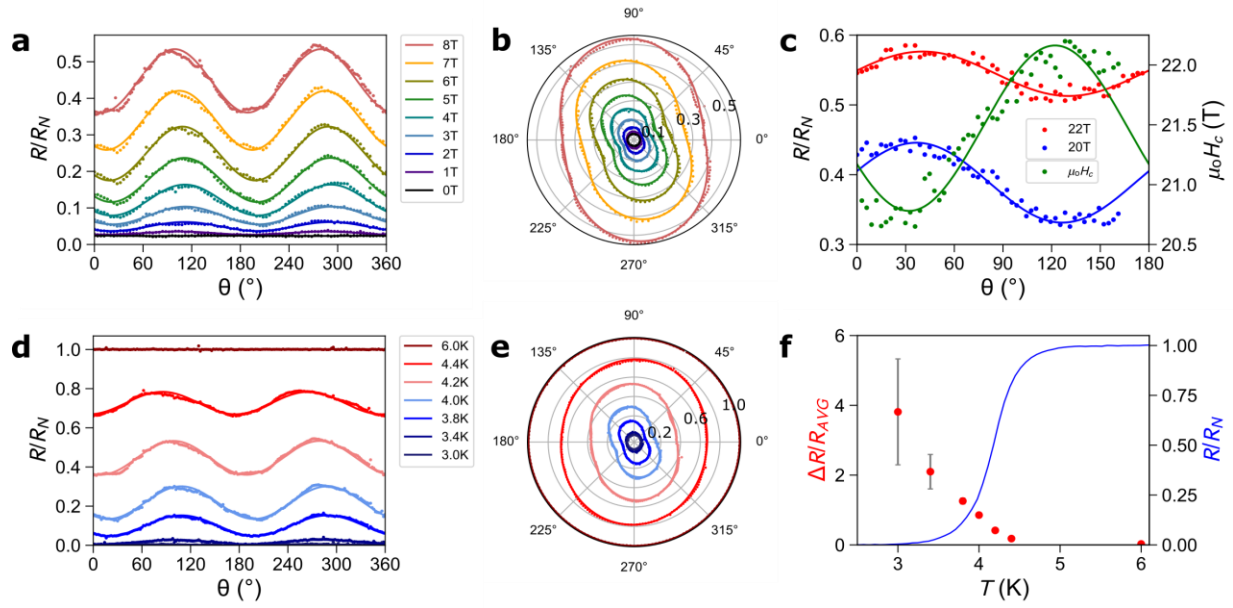


Fig. 2. Magnetoresistance and critical field signatures of twofold superconducting behavior. **a.** Field dependence ($T = 4.2\text{K}$) of magnetoresistance for Device 1. **b.** Radial plot of data in **a**; the radial scale is R/R_N . **c.** Critical field (green) and magnetoresistance characterization (blue and red) for Device 3, 5-layer NbSe_2 ($R_N = 22.2\Omega$, $T = 0.5\text{K}$). For Device 3, θ is defined with respect to an arbitrary reference. **d.** Temperature dependence ($\mu_0 H = 8\text{T}$) of magnetoresistance for Device 1. **e.** Radial plot of data in **d**. Solid lines in **a-e** are fits to a $\cos(2\theta + \varphi)$ form. **f.** Relative amplitude ($\Delta R/R_{\text{AVG}}$) of the magnetoresistance oscillations shown in **d**; the R vs. T for Device 1 in the presence of $\mu_0 H = 8\text{T}$ is plotted in blue. The error bars were calculated using conventional error propagation; the uncertainty of a single data point from **d** was defined as the standard deviation of the 6K data.

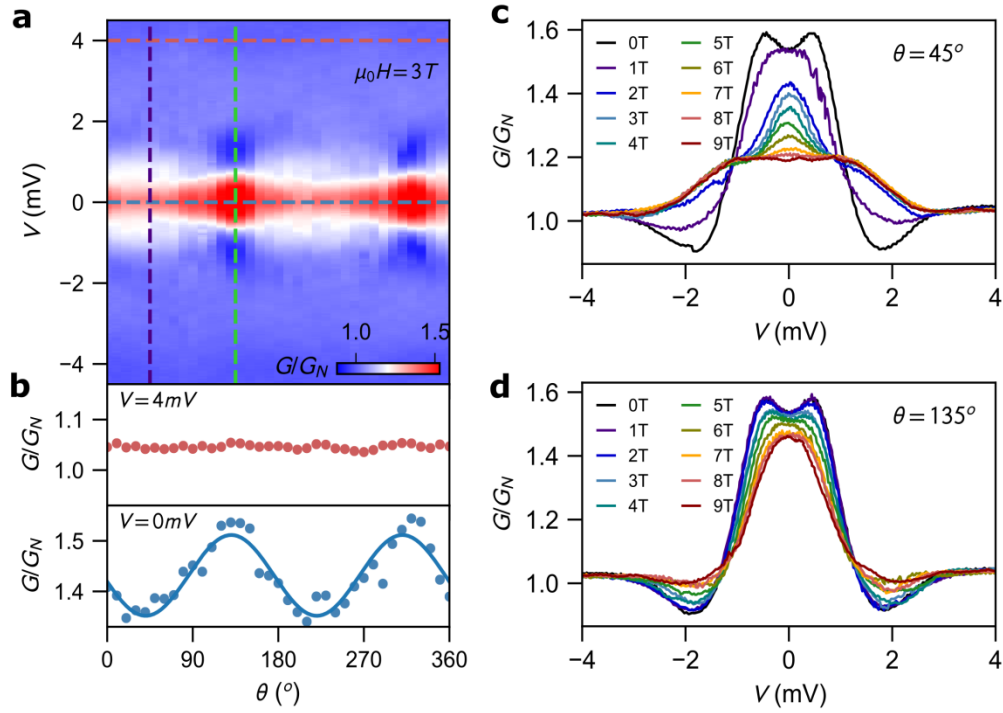


Fig. 3. Differential conductance spectra under in-plane magnetic field. **a.** Color plot of the differential conductance of trilayer NbSe₂/bilayer CrBr₃/Pt junction as a function of the angle θ of the in-plane magnetic field ($\mu_0 H = 3 T$, $T = 1.9 K$). **b.** G/G_N vs. angle at $V = 0$ and $4 mV$ (blue and red dashed lines in **a**). The solid line is the best fit to a $\cos(2\theta + \varphi)$ form. **c, d.** Field-dependent differential conductance spectra at two fixed in-plane field directions: $\theta = 45^\circ$ (**c**, purple dashed line in **a**) and 135° (**d**, green dashed line in **a**).

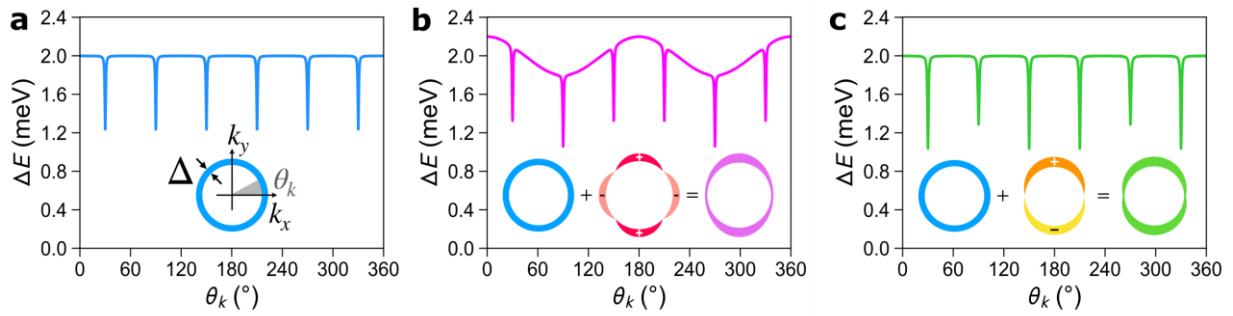


Fig. 4. Theoretical model for the two-fold anisotropic gap in NbSe₂. All gaps refer to the Γ Fermi surfaces shown in Fig. 1c; although two Fermi pockets exist, the gaps are essentially equal in both of them. **a.** A_1' (s-wave) gap function. The six-fold anisotropy is a consequence of the Ising-SOC and reflects the three-fold rotational symmetry of the lattice. **b.** Mixing of A_1' (s-wave) and E' (d-wave) gaps promoted by uniaxial strain. **c.** Mixing of A_1' (s-wave) and E'' (p-wave) gaps promoted by the in-plane magnetic field. Insets: schematics of the superconducting gaps A_1' (blue), E' (red), E'' (yellow), $A_1'+E'$ (magenta), and $A_1'+E''$ (green).

Supplementary Information

S1. Cant angle analysis

We rule out the possibility that the observed two-fold modulation might have been caused by an out-of-plane component of the applied field, which would have oscillated with the same periodicity due to an unintentional cant of the sample plane with respect to the field rotation plane. The geometry of the canted sample and pertinent parameters are shown in Figure S1.1. The perpendicular field is proportional to $|\sin(\theta + \theta_0)|$, where θ_0 is the angle needed for the field to be totally in the plane of the sample. The voltage response is also proportional to the perpendicular field for moderate R/R_N (Figure S1.2), so the voltage response to an out-of-plane field should be proportional to $|\sin(\theta + \theta_0)|$.

We carried out fits for $\sin[2(\theta + \theta_0)]$ and $|\sin(\theta + \theta_0)|$ to determine the major cause of the sample's response (Figures S1.3 a-d). Moreover, a control test was performed with the same sample, but introducing an intentional ($\sim 7^\circ$) cant by using a SiO_x chip as shim (Figures S1.3 e-h). We find that $|\sin(\theta + \theta_0)|$ fits the 7° cant data well, and the fit is clearly better than that for $\sin[2(\theta + \theta_0)]$. This demonstrates that magneto-resistance data does take on a $|\sin(\theta + \theta_0)|$ form in the presence of a tilted sample. By comparison, the data with no intentional cant (as in the main text) is fit best by $\sin[2(\theta + \theta_0)]$ and does not fit well to $|\sin(\theta + \theta_0)|$, excluding the possibility that the effects reported in the main text are due to an accidental tilt of the sample with respect to the field plane. This is further supported by our observations in one sample that the angle of minimum resistance of the twofold oscillations was affected by temperature and field modulation (Figure 2), which is inconsistent with the view of these oscillations being caused by misalignment (further covered in S3).

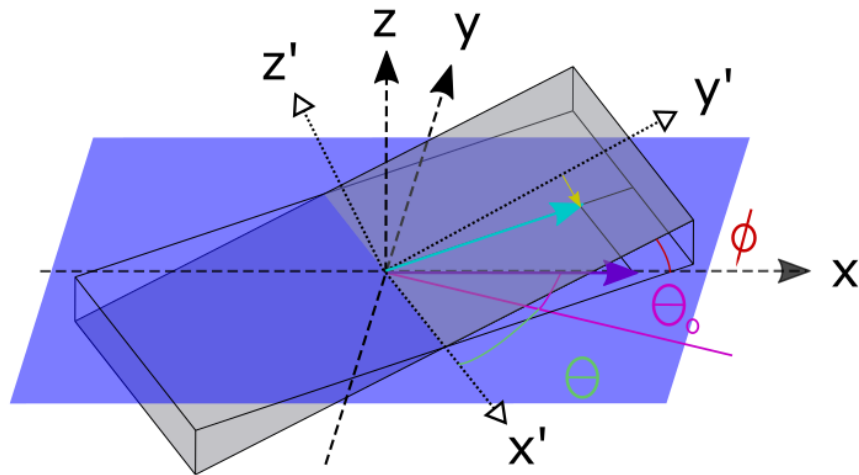


Figure S1.1. Geometry of a canted sample. The field lies in the x-y plane, and the sample in the x'-y' plane. The field component perpendicular to the plane of the sample takes the form $\mu_0 H |\sin(\theta + \theta_0)| \sin(\phi)$. Here, θ is the angle in the x-y plane, θ_0 is the angle at which the field lies entirely in the plane of the sample (x'-y'), and ϕ is the sample's cant angle from the plane in which the field rotates (angle between the x-y and x'-y' planes). The field plane is blue, and the sample plane is grey. $\mu_0 H$, $\mu_0 \sin(\theta + \theta_0)$ and $\mu_0 H |\sin(\theta + \theta_0)| \sin(\phi)$ are indicated by purple, light blue and yellow arrows, respectively.

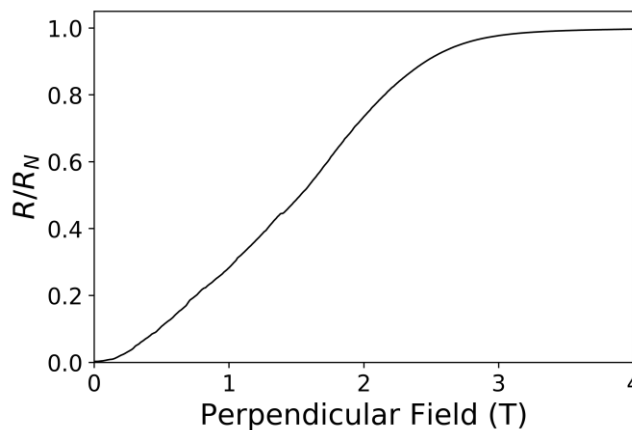


Figure S1.2. Magnetoresistance characterization for out-of-plane sweep using Device 1. For a range of moderate R/R_N , resistance is roughly linear with perpendicular field (T=1.8K).

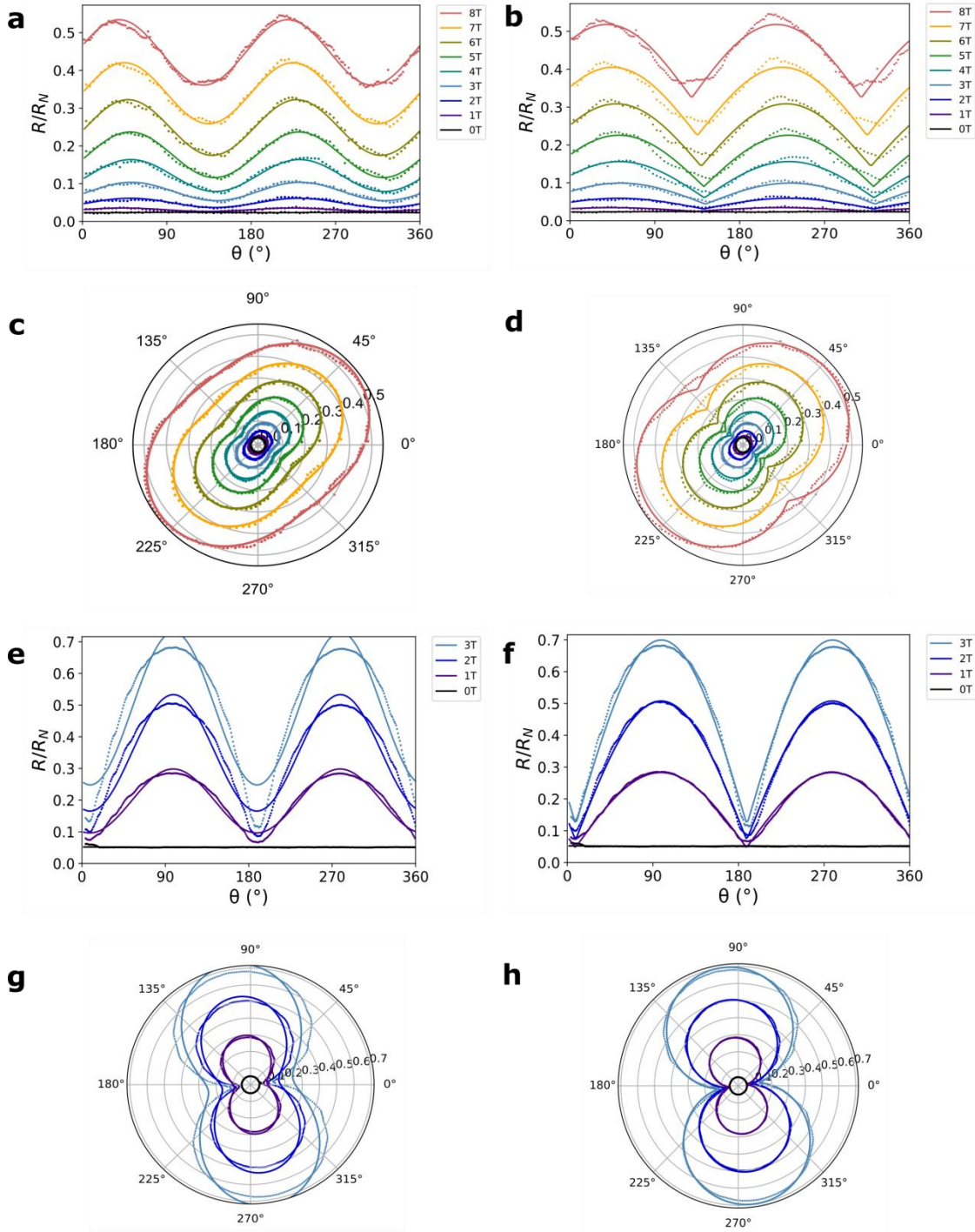


Figure S1.3. Data are qualitatively different between canted and non-canted samples. a-d: Device 1 with no cant. **e-h.:** Device 1 with intentional cant. **a, c, e, g:** Fits to $\sin[2(\theta + \theta_0)]$. **b, d, f, h:** Fits to $|\sin(\theta + \theta_0)|$. Radial axis for polar plots is R/R_N . Fits are solid curves, and experimental data are discrete points.

S2. Quantitative analysis of magneto-resistance to exclude plane misalignment

The general model for misalignment-induced magnetoresistance oscillations is shown in Figure S2a where, due to misalignment angle ϕ , the normal vector \hat{n} of the sample precesses in a cone with in-plane rotation. This would lead to resistance maxima at the two angles corresponding to max out-of-plane field, $\theta_{|\vec{H}_\perp|_{\max}}$, due to thin superconductors being more vulnerable to out-of-plane fields than in-plane fields due to vortex formation. The hypothetical ϕ was found by first measuring one sample's in-plane magnetoresistance oscillations (Figure S2b) and then directly measuring the transition curve with respect to H_\perp (Figure S2c) after changing the sample holder, re-bonding and confirming an essentially unchanged contact resistance. By examining the voltage fluctuations at the temperature matching that used for the transition curve, one can estimate the associated max out-of-plane field if the oscillations were due to misalignment. Comparing this to the applied field in S2b, one gets an associated misalignment $\phi \sim 2.44^\circ$, which is much higher than what is expected to be realistic for our measurement setup. Image analysis showed an estimated ϕ on the order of tenths of a degree, thus being approximately one order of magnitude smaller than that capable of explaining our data. In addition, the hBN-SiO₂ and hBN-NbSe₂ interfaces are unlikely to host this misalignment due to the associated nm-scale topographic variation and μm length scale of the sample.

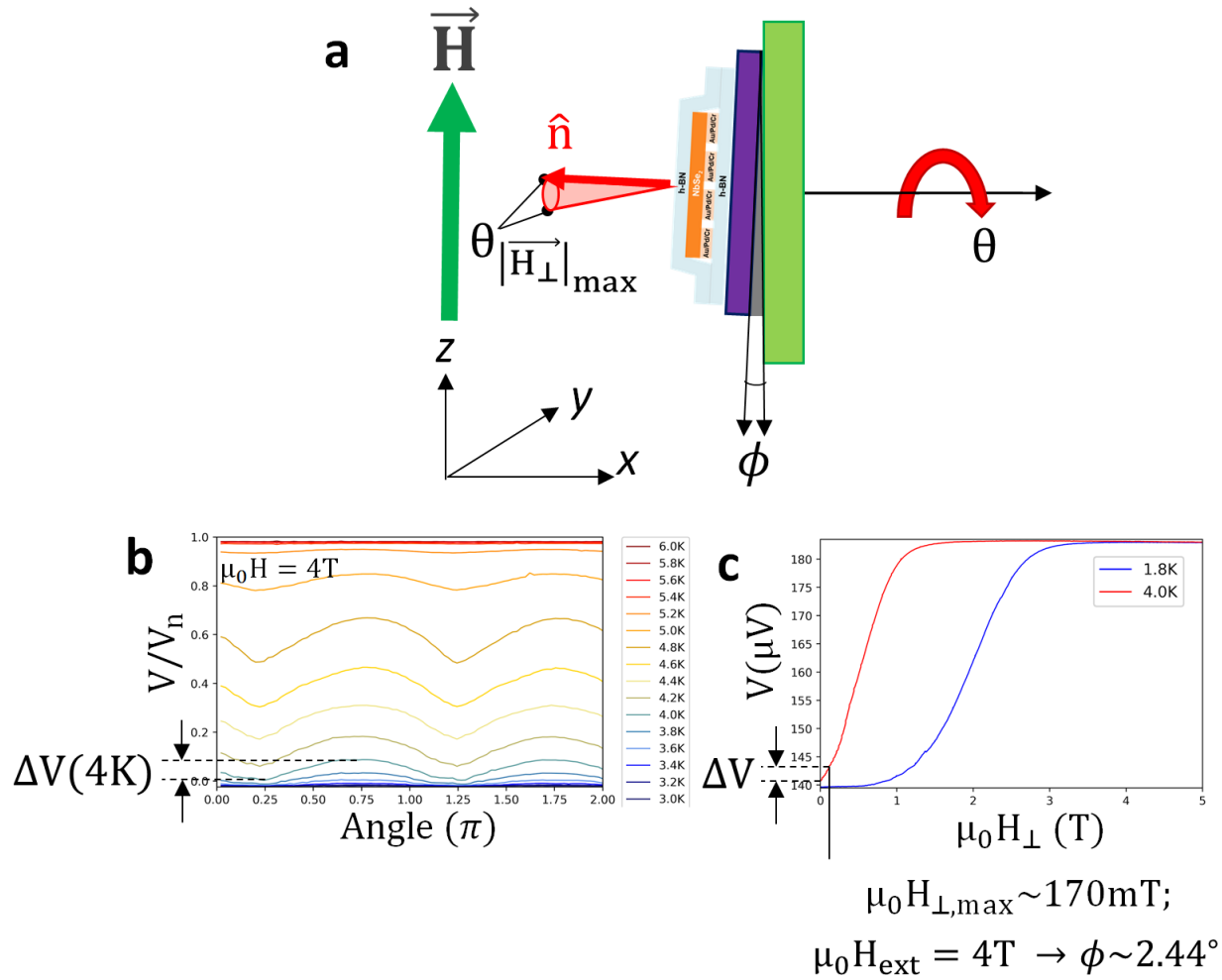


Figure S2. Quantitative analysis of magneto-resistance to exclude plane misalignment. **a.** Schematic showing geometry of setup with sample cant angle of ϕ . **b.** Temperature-dependent data from Device 1 in an in-plane 4T field. **c.** Magneto-resistance of out-of-plane field sweep (three-point measurement using an a.c. current of $1\mu\text{A}$).

S3. Shifting minima

Another piece of evidence against an out-of-plane effect was a shifting minimum angle in the data. For a purely out-of-plane effect, no shift should be expected – this is confirmed in Figure S3 for the canted Device 1, whose minima had a range of 4° (the resolution of the measurement). Instead, Device 1 without a cant showed a minimum range of 16° for temperature dependence with a general trend to the left, and the field dependence shows a range of 32° . Notable is that this phase shift with both temperature and field modulation implies a dependence on location along the superconducting transition, rather than being due to extrinsic effects.

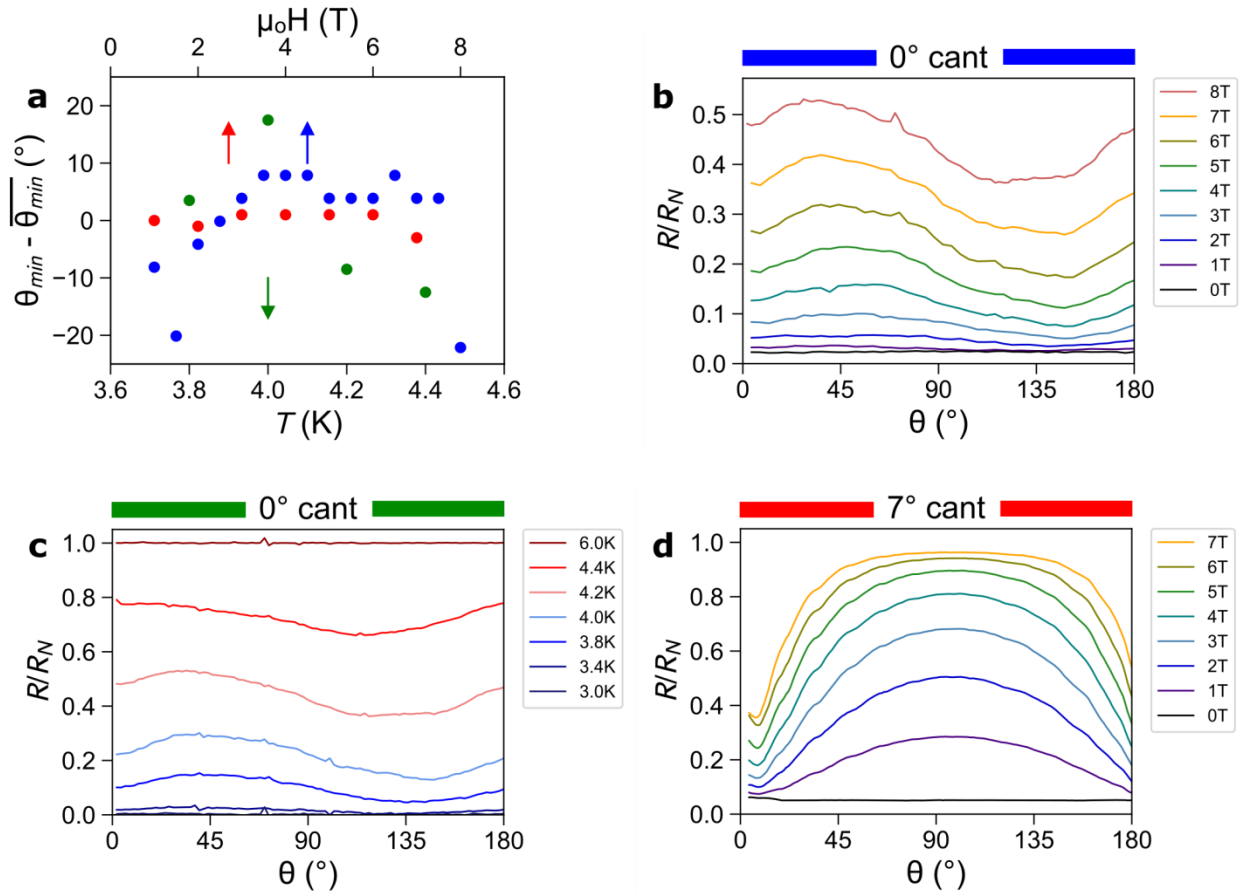


Figure S3. Magnetoconductance minimum shift present for 0° cant, absent for 7° cant. **a.** Angle at which minimum of magnetoconductance occurs for the three cases shown in panels **b-d**, centered around each set's average minimum angle. **b.** Field dependence of Device 1 with 0° cant (average minimum: 144°). **c.** Temperature dependence of Device 1 with 0° cant (average minimum: 133°). **d.** Field dependence of Device 1 with 7° cant (average minimum: 10°). The minimum for the 7° cant shifts very little (almost not at all) compared to that of the 0° cant. Note: the data for the 0° cant is the raw data of that shown in the main text.

S4. Characterization of Device 3.

Device 3 was made from a 5-layer NbSe₂ sample, the same as Device 1. The R vs. T (Figure S4a) for this sample showed an R_N of 20.4Ω and $T_c \approx 6.2$ K. This gives a superconducting gap $\Delta \approx 1.76k_B T_c \approx 0.94$ meV. Although the transition width is wider than in Device 1 and less uniform at low resistances, the magnetoresistance and critical field data were taken at a smooth part of the transition ($\sim 0.35R_N$ to $\sim 0.6R_N$) and showed no anomalies.

Resistance dependence on perpendicular and parallel fields were also studied at 0.5K (Figure S4b). The out-of-plane critical field was ~ 4 T, and the in-plane critical field was ~ 27 T. These two measurements were taken on the same holder, and immediately following one another, but with the holder turned 90° from the first to second measurement such that the rotation in-plane with the field became a rotation out-of-plane.

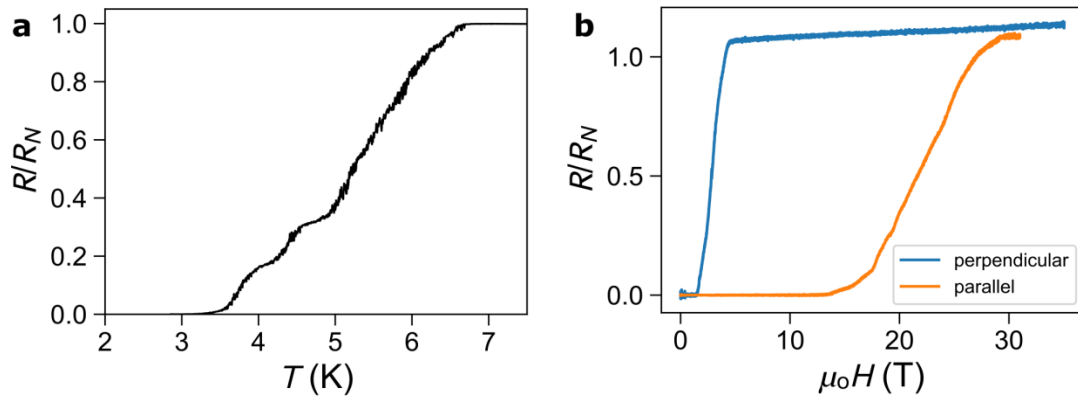


Figure S4. Characterization for Device 3. a. Normalized R vs. T. b. Normalized R vs. magnetic field for both when the field and sample plane are parallel and perpendicular. $R_N = 20.4\Omega$.

S5. Directional Analysis of Magnetotransport across multiple devices.

Directions of current, voltage drop, and that of the magnetic field associated with resistance extrema are shown in Figures S5a-c, with additional images of the corresponding NbSe₂ flakes as guides to the eye when needed. It can be seen that the direction of the current and voltage drop show no correspondence with the field direction of minimum resistance $\hat{H}_{R\min}$. However, examination of $\hat{H}_{R\min}$ across all samples shows a repeated alignment with the long, straight edge of the NbSe₂ flakes. Figure S5d shows the associated magnetoresistance oscillations used for each device to determine the orientation of $\hat{H}_{R\min}$.

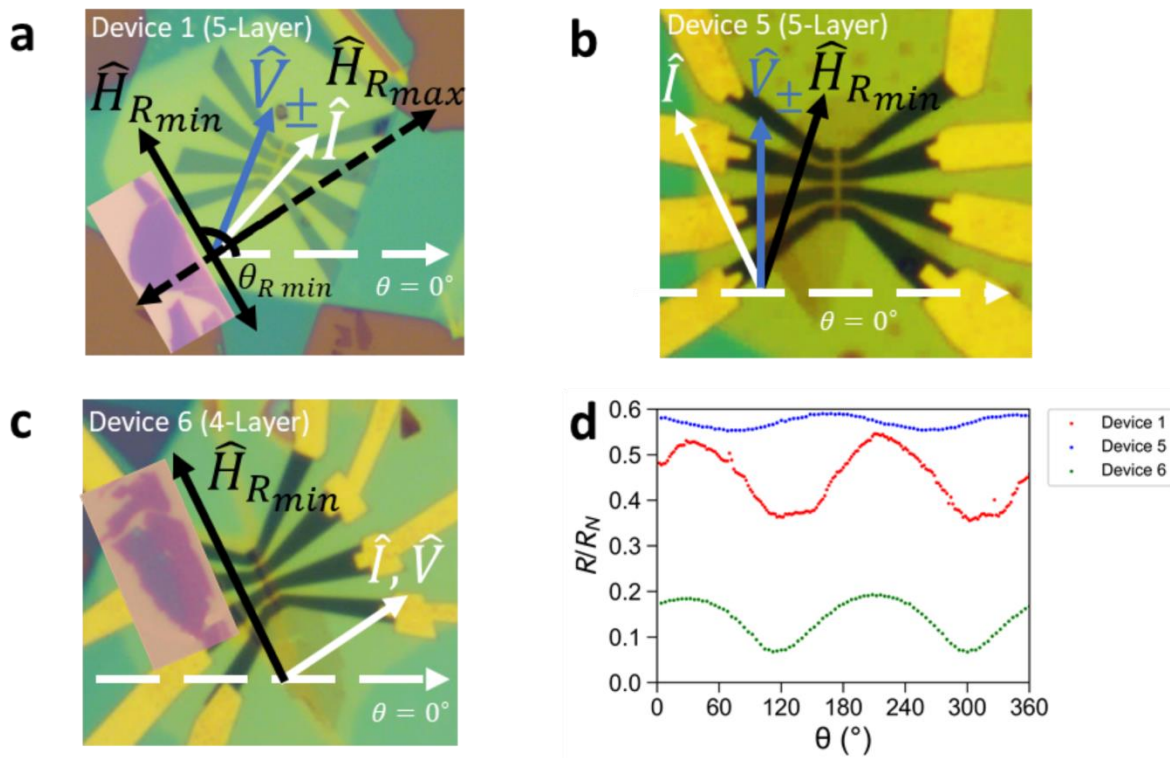


Figure S5. Directional analysis of magnetotransport across several devices. a.-c. Device images of Devices 1, 5, and 6 along with the associated direction of the field of minimum resistance as well as the current and voltage directions. Pictures of the NbSe₂ flakes are provided as guides to the eye as needed. In Device 1, the associated field of maximum resistance is provided as well as an example. d. Plot of the magnetoresistance oscillations used for each device for determination of $\hat{H}_{R\min}$. The angle of minimum resistance for Devices 1, 5, and 6 correspond to 122°, 68°, and 120° respectively.

S6. Differential conductance measurement schematics

Figure S6 shows the setup for measuring the differential conductance of the junction highlighted by a red square. We use a lock-in amplifier and voltage source meter as the a.c. and d.c. voltage source, respectively. Each instrument is connected to a load resistance to convert the voltage signal to a current signal. A typical d.c. and a.c. load resistance is $100\text{ k}\Omega$ and $1\text{ M}\Omega$, respectively. The superimposed a.c. and d.c. current is fed to one of the split electrodes. The a.c. and d.c. voltage signal is measured between the other split electrode and another remote electrode. The differential conductance is defined as the ratio of the applied ac current to the measured ac voltage. We normalize the differential conductance G to the zero bias differential conductance in the normal metal state G_N measured at $T \approx 5.8\text{ K}$. All spectra reported are plotted in terms of G/G_N vs. the measured d.c. bias voltage.

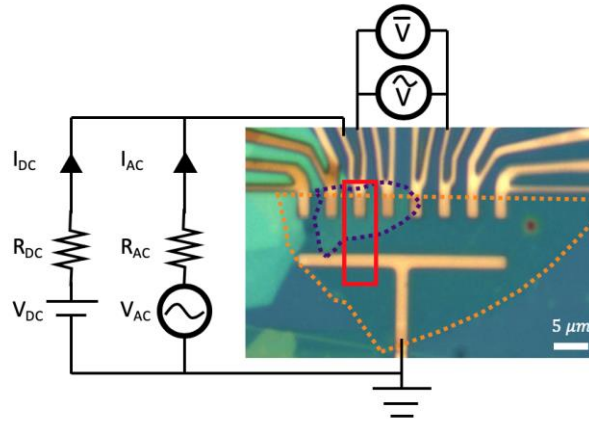


Figure S6. Schematic of differential conductance measurement.

S7. Differential conductance measurements on Device 4

We present a second device which is constructed with a magnetic metal electrode (multilayer Co/Pt) which shows identical results as the one introduced in the main text. Pre-patterned magnetic metal electrodes are prepared by standard photolithography on a Si/SiO₂ (290 nm) substrate and e-beam evaporation of 3 nm Ti/10 nm Pt/(0.3 nm Co/1 nm Pt)×8/0.5 nm Co/2.5 nm Au/0.4 nm AlO_x. Multilayer Co/Pt is a ferromagnetic metal with an easy-axis in the out-of-plane direction [S1]. The measured saturation field for the out-of-plane and in-plane direction is ~0.5 T and ~0.8T, respectively. The 2.5 nm Au prevents oxidation of Co and the 0.4 nm AlO_x layer serves as an insulating barrier. A trilayer NbSe₂ flake and a h-BN protection layer is transferred in sequence on to the prepatterned substrate by the standard dry transfer technique (Figure S7a). The normal state resistance of the junction is $R_N = 11 \Omega$ which is more than an order of magnitude smaller than the CrBr₃ barrier device.

We repeat the measurement as introduced in the main text. An in-plane magnetic field of 3T is applied which saturates magnetic moment of the Co/Pt electrodes in the in-plane direction. Differential conductance spectra are acquired as the magnetic field is rotated in the in-plane direction. The results are summarized in Figure S7b. Consistent to the main text, there is a two-fold dependency of the spectra in terms of the angle θ . The zero-bias normalized conductance G/G_N vs. angle θ shows a $\cos(2\theta)$ dependence while at larger bias the dependency is weak. When the in-plane field is fixed in $\theta = 90^\circ$, the differential conductance within the gap suppresses quickly in larger field, similar to Figure 3c in the main text. On the other hand, when the field is directed in $\theta = 160^\circ$, the tunneling spectra is more robust showing little suppression to the gap like that observed in Figure 3d. We find that tunneling to NbSe₂ either through a magnetic insulating barrier or from a magnetic electrode results in a two-fold modulation in the tunneling spectra.

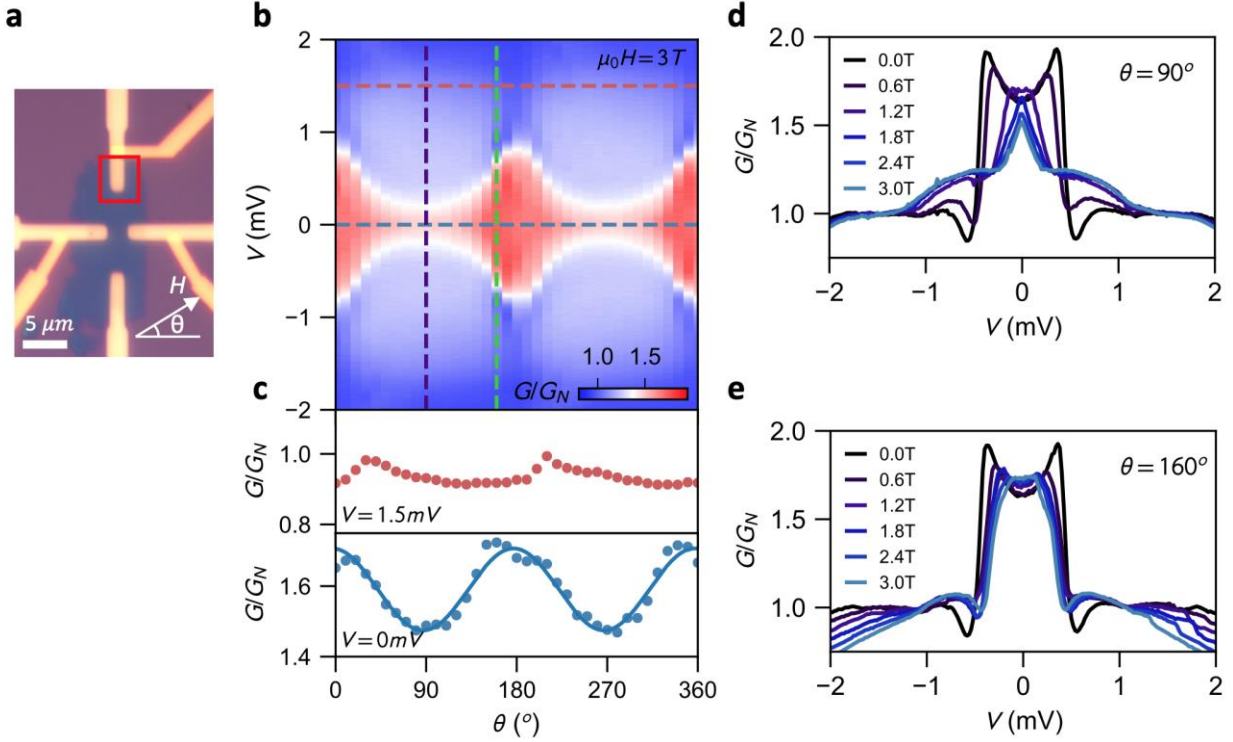


Figure S7. Differential conductance measurement on Device 4. **a.** Optical image of Device 4. The visible prepatterned electrodes are multilayers of Co/Pt. The blue flake is a trilayer NbSe₂ and the covering h-BN is not shown in this image. The in-plane magnetic field angle θ is defined as illustrated. **b.** Contour plot of the differential conductance spectra under in-plane magnetic field at 2.3 K. **c.** G/G_N vs. angle at $V = 0$ and 1.5 mV (blue and red dashed lines in **b**). The solid line is the best fit to a $\cos(2\theta)$ form. **d, e.** Field-dependent differential conductance spectra at two fixed in-plane field directions: $\theta = 90^\circ$ (**d**, purple dashed line in **b**) and 160° (**e**, green dashed line in **b**).

S8. Phenomenological Description of Superconducting Anisotropy in NbSe₂

Since we expect the behavior of few-layer NbSe₂ to be representative of the monolayer compound, as long as the inter-layer coupling is weak, we consider the point group of the latter, which is D_{3h} . This point group is non-centrosymmetric, reflecting the fact that it incorporates the effects of the Ising spin-orbit coupling (SOC).

The possible superconducting gaps, which we denote $\tilde{\Delta}_{\Gamma, m}^{(\alpha)}$, can be classified based on the irreducible representation Γ of D_{3h} under which they transform, as well as whether they correspond to spin-singlet ($\alpha = s$) or to spin-triplet ($\alpha = t$) Cooper pairs. When Γ is not 1-dimensional, we use the index m to distinguish different components of the corresponding multiplet. We note that since D_{3h}

incorporates Ising SOC, a given Γ contains both singlet and triplet gap components, and the solutions of the superconducting gap equation are a mixture of spin-singlet and spin-triplet Cooper pairs^{12,14,24}

Γ	m	$\Theta_{\Gamma,m}^{(s)}(\mathbf{p})$	$\Theta_{\Gamma,m}^{(t)}(\mathbf{p})$
A_1'	1	$i\sigma^y$	$\cos 3\theta \sigma^z i\sigma^y$
E'	1	$\cos 2\theta i\sigma^y$	$\cos \theta \sigma^z i\sigma^y$
	2	$\sin 2\theta i\sigma^y$	$\sin \theta \sigma^z i\sigma^y$
E''	1		$\cos 3\theta \sigma^x i\sigma^y, (\cos \theta \sigma^x - \sin \theta \sigma^y) i\sigma^y$
	2		$\cos 3\theta \sigma^y i\sigma^y, (\sin \theta \sigma^x + \cos \theta \sigma^y) i\sigma^y$

Table S8.1. Irreducible representations of D_{3h} relevant to our analysis. We exclude irreps that vanish in the monolayer ($p_z = 0$) limit. The singlet component of A_1' E' can be associated to an s -wave (d -wave) gap, while the lowest harmonic in the triplet E'' irrep can be associated with a p -wave order parameter. Here we take one of the K points to lie along the p_x axis, i.e. $\theta = 0$.

Here we focus on the Γ pocket (not to be confused with the irrep index), since we expect the gap associated with $\pm K$ pockets to be isotropic¹⁴. The corresponding superconducting gap $\tilde{\Delta}(\mathbf{p})$ can then be expressed as:

$$\tilde{\Delta}(\mathbf{p}) = \sum_{\Gamma\alpha m} \Theta_{\Gamma,m}^{(\alpha)}(\mathbf{p}) \Delta_{\Gamma,m}^{(\alpha)} \quad (1)$$

where $\Delta_{\Gamma,m}^{(\alpha)}$ is a complex scalar parameterizing the magnitude of the contribution to the superconducting gap from the irrep Γ , in pairing channel α . We take $\Theta_{\Gamma,m}^{(\alpha)}(\mathbf{p})$ to be functions of only the angle θ with respect to the Brillouin zone center. Note that by particle hole symmetry, $\tilde{\Delta}(\mathbf{p}) = -\tilde{\Delta}^T(-\mathbf{p})$, which implies that $\Theta_{\Gamma,m}^{(s)}(\mathbf{p})$ ($\Theta_{\Gamma,m}^{(t)}(\mathbf{p})$) is an even (odd) function of \mathbf{p} .

The irreps relevant to our analysis here are shown in Table S8.1. To make a connection with the usual classification of gaps in isotropic space, we note that these are an s -wave singlet gap and f -wave triplet gap in the A_1' irrep; a d -wave singlet and a p -wave triplet in the E' irrep; and p - or f -wave triplets in the E'' irrep. We have omitted most irreps corresponding to gaps that are non-uniform on the K

pockets, which do not contribute to the leading-order superconducting instabilities.¹⁴ The exception is the E' irrep, which we keep because it couples to A_1' by strain, and the p -wave gap in the E'' irrep, which can couple to the magnetic field, as these can generate a two-fold anisotropy in the superconducting gap. We have also kept only irreps relevant to the monolayer limit (i.e. independent of the \hat{z} direction).

A few remarks are in order. First, because of the Ising spin-orbit coupling, the A_1' and E' irreps contain both singlet and triplet gaps. The E'' irrep, however, contains only triplet components as the corresponding singlet gap cannot be realized in a \hat{z} -independent way. Second, the E' and E'' irreps are 2-dimensional, leading to two degenerate solutions to the gap equation.

In order to determine the form of the superconducting gap in the presence of strain and a magnetic field, we use a phenomenological approach, analyzing what terms quadratic in the superconducting gaps are allowed in the Ginzburg-Landau free energy. Within this approach the functional form of the gap is not determined, only the relative weights of each irrep. In practice, one of the terms within a given irrep in Table S8.1 is usually dominant, and the rest can be dropped (which term is relevant is not determined within this approach). Here we focus on terms involving the singlet component of the gap in the A_1' (s -wave) channel, which we expect to be large compared to its triplet counterpart, and similarly assume that only one of any of the terms in the E' and E'' irreps is relevant. We focus on the singlet d -wave term in E' and the triplet p -wave term in E'' as those give rise to the two-fold anisotropy in the spectrum. We can therefore drop the superscript on the coefficients in front of the gap function within a given irrep and label them as $\Delta_{A_1'}$, $\Delta_{E'}$, and $\Delta_{E''}$, where the latter are 2-component vectors representing the doublet.

We assume that the dominant superconducting instability is in the A_1' irrep, which contains singlet s -wave terms. Near the superconducting transition temperature (in the absence of a magnetic field or strain), the free energy has the form

$$\mathcal{F}_0 = \mathcal{F}_0[\Delta_{A_1'}] + \frac{1}{2}(\chi_{E'}^{-1}(T)|\Delta_{E'}|^2 + \chi_{E''}^{-1}(T)|\Delta_{E''}|^2) . \quad (2)$$

Here $\chi_\Gamma(T) \propto 1/(T-T_{c,\Gamma})$ is the susceptibility associated with superconducting fluctuations in the Γ irrep, with $T_{c,\Gamma}$ being the corresponding transition temperature. We leave here the precise form of $\mathcal{F}_0[\Delta_{A_1'}]$ unspecified. Our main assumption is that the leading superconducting instability takes place at a temperature $T_{c,A_1'}$ that is larger than $T_{c,E'}$ and $T_{c,E''}$.

In the presence of perturbations such as strain and magnetic field, which do not respect the D_{3h} symmetry, additional terms in the free energy that mix the different irreducible representations at quadratic order in the $\Delta_{\Gamma,m}$ are allowed. We consider two mixing terms that can lead to a twofold anisotropy in the superconducting gap.

First, since the in-plane magnetic field \mathbf{b} (in units of the Bohr magneton times the Landé g -factor, $\mathbf{b} = g_L \mu_B \mathbf{B}$) transforms according to the E'' irrep and the Ising spin-orbit coupling vector $\lambda p_F^3 \cos 3\theta \hat{\mathbf{z}}$ transforms according to A_1' , a singlet A_1' -triplet E'' mixing term of the form $\lambda p_F^3 \Delta_{A_1'} \mathbf{b} \cdot (\hat{\mathbf{z}} \times \Delta_{E''})$ is allowed, consistent with the results of Ref. 23. The resulting term in the free energy is

$$\mathcal{F}[\Delta_{A_1'}, \Delta_{E''}] = \lambda_1 \text{Re} \left[\Delta_{A_1'}^* (b_y \Delta_{E'',1} - b_x \Delta_{E'',2}) \right]. \quad (3)$$

where λ_1 is some coupling constant proportional to λ . Minimizing the resulting free energy with respect to $\Delta_{E'',m'}$, we find that

$$(\Delta_{E'',1}, \Delta_{E'',2}) = -\lambda_1 \chi_{E''} \Delta_{A_1'} (b_y, -b_x) \quad (4)$$

and the total superconducting gap is

$$\tilde{\Delta}(\mathbf{p}) = \Delta_{A_1'} [\theta(\mathbf{p}) - \lambda_1 \chi_{E''} \Theta_{E''}(\mathbf{p}) \cdot (\hat{\mathbf{z}} \times \mathbf{b})] \quad (5)$$

which is a mixture of the s -wave singlet A_1' gap and the p -wave triplet E'' gap. The magnitude of $\Delta_{E''}$ (relative to that of $\Delta_{A_1'}$) is set by the coefficient $\lambda_1 \chi_{E''} |b|$. Since the magnetic field b is a small perturbation, generically we expect this coefficient to be small, and the corresponding mixing to be weak. However, if $T_{c,E''}$ is comparable to $T_{c,A_1'}$, then in the vicinity of $T_{c,A_1'}$ the susceptibility $\chi_{E''}(T) \sim 1/(T_{c,A_1'} - T_{c,E''})$ is very large. Thus we expect that weak magnetic fields can lead to appreciable mixing between the s -wave singlet and the p -wave triplet only when $T_{c,A_1'}/T_{c,E''}$ is close to 1 – i.e. only when these two superconducting instabilities are close competitors.

Second, the strain combination $\mathcal{E} = (\varepsilon_{xx} - \varepsilon_{yy}, 2\varepsilon_{xy})$ transforms according to the E' irreducible representation. Here, $\varepsilon_{ij} \equiv \frac{1}{2}(\partial_i u_j + \partial_j u_i)$ is the strain tensor and \mathbf{u} is the displacement vector. This leads to a coupling between the singlet components of the A_1' and E' gaps of the form:

$$\mathcal{F}[\Delta_{A_1'}, \Delta_{E''}] = \lambda_2 \left[(\varepsilon_{xx} - \varepsilon_{yy}) \text{Re} \left(\Delta_{A_1'}^* \Delta_{E',1} \right) + 2\varepsilon_{xy} \text{Re} \left(\Delta_{A_1'}^* \Delta_{E',2} \right) \right]. \quad (6)$$

where λ_2 is some coupling constant. Minimizing the free energy leads to a mixed s -wave and d -wave superconducting gap

$$\tilde{\Delta}(\mathbf{p}) = \Delta_{A_1'} [\Theta_{A_1'}(\mathbf{p}) - \lambda_2 \chi_{E'} \Theta_{E'} \cdot \boldsymbol{\varepsilon}] \quad (7)$$

Again, small strains will only lead to a significant E' component in the superconducting gap if the A_1' and E' superconducting instabilities have similar transition temperatures.

Fig. 4 of the main text shows the resulting 2-fold anisotropy in the superconducting gap around the Γ pocket. We obtained the plots using a simple model of the single-body Hamiltonian in momentum space:

$$H(\mathbf{p}) = \sum_{\mathbf{p}s} \varepsilon(\mathbf{p}) c_{\mathbf{p}s}^\dagger c_{\mathbf{p}s} + \sum_{\mathbf{p}ss'} c_{\mathbf{p}s}^\dagger [\lambda p_F^3 \cos 3\theta \sigma^z + \mathbf{b} \cdot \boldsymbol{\sigma}]_{ss'} c_{\mathbf{p}s'} = \sum_{\mathbf{p}ss'} c_{\mathbf{p}s}^\dagger [\mathcal{H}_0]_{ss'} c_{\mathbf{p}s'} \quad (8)$$

where s and s' are spin indices,

$$\varepsilon(\mathbf{p}) = -\frac{p^2}{2m} - \mu, \quad (9)$$

and θ , as above, is the angle measured from the center of the Γ pocket with $\theta = 0$ corresponding to the direction towards the K point. We use $\lambda p_F^3 = 40$ meV, which is the Ising SOC value reported in the literature once averaged over all Fermi surfaces²². We also set $\mu = 0.4$ eV, which gives $m = p_F^2/2\mu \approx 2m_0$ when the wavenumber corresponding to the Fermi momentum is $p_F/\hbar = 0.45 \text{ \AA}^{-1}$ [S2]. Here, m_0 is the electron rest mass. All these parameters were chosen so that the Fermi surface of the toy-model parabolic dispersion is similar to that obtained from first principle calculations^{12,22,24}. These values should thus not be understood as actual parameters that a first-principle calculation would yield. The key point is that our conclusions do not rely on this set of parameter values, as they are used to illustrate the two-fold gap anisotropy that must follow from mixing an A_1' gap with either E' or E'' gaps. Finally, for the magnetic field, we use $b = 1$ meV, which is about 8.3 T.

The superconducting excitation spectrum is then given by the eigenvalues of the Bogolyubov-de Gennes (BdG) Hamiltonian:

$$H_{BdG} = \frac{1}{2} \sum_{\mathbf{p}} \Psi_{\mathbf{p}s}^\dagger \mathcal{H}(\mathbf{p}) \Psi_{\mathbf{p}s'} \quad (10)$$

where we use the Nambu-Gor'kov representation $\Psi_{\mathbf{p}s} = (c_{\mathbf{p}s}, c_{-\mathbf{p}s}^\dagger)^T$ and

$$\mathcal{H}(\mathbf{p}) = \begin{pmatrix} \mathcal{H}_0(\mathbf{p}) & \tilde{\Delta}(\mathbf{p}) \\ \tilde{\Delta}^\dagger(\mathbf{p}) & -\mathcal{H}_0^T(-\mathbf{p}) \end{pmatrix}. \quad (11)$$

We took $\tilde{\Delta}(\mathbf{p})$ as in Eqs. (5) and (7). We took the singlet d -wave term for E' and the triplet p -wave term for E'' from Table 1. For all plots, we took $\Delta_{A_1'} = 2$ meV. For the mixed A_1'/E' gaps, we took $|\Delta_{E'}| = 0.2$ meV and an uniaxial strain along the x axis, $\mathcal{E} \propto (1,0)$. For the mixed A_1'/E'' gap, the mixing is relatively weak unless the mixed gaps are close in magnitude; for this reason, we used $|\Delta_{E''}| = 1$ meV in the plot. Note that we plot the energy gap in the spectrum of H_{BdG} (i.e. difference between bottom positive energy band and top negative energy band) along both the inner and outer Fermi surfaces. The resulting gaps on the inner and outer surfaces are identical within the resolution of the figure.

A second potential source of anisotropy comes from the spatial variations of the doublet gaps in the E' and E'' irreps, i.e. from the gradient terms of the Ginzburg-Landau free-energy. For the one-component A_1' irrep, the only allowed gradient term is of the form $\mathcal{F}_{\nabla}^{(A_1')} = K_0 |\nabla D^{(0)}|^2$, which is clearly rotationally invariant. For the doublet E' and E'' representations, however, the possible terms in \mathcal{F} involving gradients of the gap functions are [S3].

$$\mathcal{F}_{\nabla}^{(\Gamma)} = K_1 |\nabla \cdot \mathbf{\Delta}_{\Gamma}|^2 + K_2 |\nabla \times \mathbf{\Delta}_{\Gamma}|^2 + K_3 (|\partial_x \Delta_{\Gamma,1} - \partial_y \Delta_{\Gamma,2}|^2 + |\partial_x \Delta_{\Gamma,2} + \partial_y \Delta_{\Gamma,1}|^2) \quad (12)$$

where $\Gamma = E', E''$. These terms can be understood as corresponding to the scalar, (axial) vector, and tensor components of the total derivative $\nabla \mathbf{\Delta}$, assuming no z dependence. Fourier transforming this expression, it follows that, in the presence of an external symmetry-breaking field such as strain, the total gradient term is also twofold anisotropic⁴⁰.

References:

- [S1]: C.-J. Lin, G.L. Gorman, Ch.H. Lee...H. Notarys, C.J. Chen. Magnetic and structural properties of Co/Pt multilayers. *J. Magn. Magn. Mater* **93**, 194 (1991).
- [S2]: Borisenko, S. V. *et al.* Two energy gaps and fermi-surface 'arcs' in NbSe2. *Phys. Rev. Lett.* **102**, 166402 (2009).
- [S3]: Sigrist, M. & Ueda, K. Phenomenological theory of unconventional superconductivity. *Rev. Mod. Phys.* **63**, 239–311 (1991).